Towards Continuous Acoustic Soft Tactile Sensing

Vishnu Rajendran S[1], Simon Parsons[2] and Amir Ghalamzan E.[1]

***Abstract*— Acoustic Soft Tactile (AST) skin is a novel sensing technology that uses deformations of the acoustic channels beneath the sensing surface to predict static normal forces and their contact locations. AST skin functions by sensing the changes in the modulation of the acoustic waves travelling through the channels as they deform due to the forces acting on the skin surface. Our previous study tested different AST skin designs for three discrete sensing points and selected two designs that better predicted the forces and contact locations. This paper presents a study of the sensing capability of these two AST skin designs with continuous sensing points with a spatial resolution of 6 mm. Our findings indicate that the AST skin with a dual-channel geometry outperformed the single-channel type during calibration. The dual-channel design predicted more than 90% of the forces within a $\pm$ 3 N tolerance and was 84.2% accurate in predicting contact locations with $\pm$ 6 mm resolution. In addition, the dual-channel AST skin demonstrated superior performance in a real-time pushing experiment over an off-the-shelf soft tactile sensor. These results demonstrate the potential of using AST skin technology for real-time force sensing in various applications, such as human-robot interaction and medical diagnosis.**

Keywords: acoustics, soft robotics, tactile sensing, robot manipulation

I. INTRODUCTION

Tactile information is vital for a robot manipulator to perform complex manipulation tasks [1]. The lack of tactile sensing makes it difficult for a manipulator to achieve dexterity comparable to that of the human hand [2]. This understanding has resulted in the integration of various tactile sensing technologies into the manipulator counterparts. As end effectors play a vital role in in-hand manipulation, greater emphasis is placed on providing tactile sensing capability to the end effectors [3].

Soft tactile sensors are preferred when force control is required to handle delicate objects using robot end effectors. Their sensing surface is composed of soft deformable materials, and they provide two functions: (i) providing a soft contact surface and (ii) converting the contact forces into noticeable deformations. They then uses electronic (e.g., resistive [4], capacitive [5], piezoelectric [6], magnetic [7], impedance [8]) and non-electronic principles (e.g., camera-based [9], [10], [11], [12], [2], fluid-based [13], and acoustics [14], [15], [16], [17]) or their combinations [18] to quantify these deformations into useful tactile information. When electronic circuits are used as tactile sensory pickups, their close-knit arrangement under sensory skin requires sophisticated manufacturing techniques. Moreover, such embedded electronics are subject to crosstalk [19]. While considering camera-based soft tactile sensors, their overall form factor hinders their usability in applications where space is a constraint. The camera size and its associated optical arrangements behind the sensing surface limit the possibility of size reduction. However, fluid-based soft tactile sensors offer delayed responses to tactile interactions [19]. In addition, they require fluid flow control valves and other accessories, which make the overall system bulky.

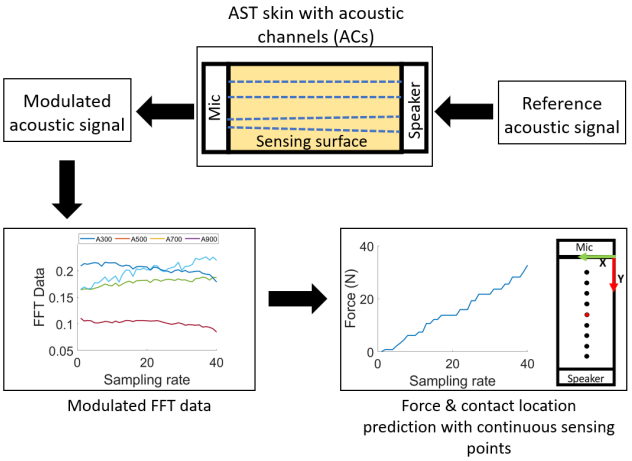

Fig. 1: Overview of AST skin technology

Compared to all these sensing principles, the acoustic method offers the freedom to use minimal hardware with less computational costs to extract rich tactile information from sensing surface deformations. This capability was demonstrated by sensorizing a flexible pneumatic finger with a single speaker and mic unit [20], [21]. Moreover, if the acoustic transmitter and receiver unit can be placed away from the sensing surface, we can develop standalone compact skins of any form factor that can be easily fitted to existing hardware (e.g., end effectors) where space is a constraint. These factors inspired us to use the acoustic principle to develop a scalable sensing skin.

We demonstrate an Acoustic Soft Tactile (AST) skin with embedded acoustic channel(s) whose deformation modulates the acoustic waves traveling through them when external force acts on the skin surface. This modulation is then mapped to the contact force and its location, which causes skin deformation (refer Fig 1). This skin technology can overcome some of the drawbacks of current soft tactile sensing methods, such as (i) ease in manufacturing, as it does not require any complex integrated electronic circuits for

*This work was supported by Lincoln Agri-Robotics as part of the Expanding Excellence in England (E3) Programme

[1] Lincoln Institute of Agri-Technology (LIAT), University of Lincoln, Lincoln, UK

[2] School of Computer Science, University of Lincoln, Lincoln, UK

tactile measurements, (ii) sensor skin can be made compact and superimposed on location with space constraints as the acoustic hardware can be placed elsewhere, (iii) skin can be made to any form factor and shape as long as it is possible to have acoustic channels beneath the sensing surface (iv) moreover, with all these possibilities, AST skin offers real-time sensing capabilities.

We evaluated the tactile sensing capabilities of several AST skin designs [22]. However, this study was limited to three discrete sensing points on the skin surface at a resolution of 20 mm.

In this paper, we study the performance of AST skin by considering continuous sensing points with a 6 mm spatial accuracy. This study will help to realise if AST skin technology can be extended as C-AST, which is the skin with continuous sensing points at this target spatial resolution. We will study the possibility of enabling 2D sensing points with a much finer resolution in the future.

II. Towards Continuous Acoustic Soft Tactile Skin (C-AST skin)

The AST skin consists of hollow Acoustic Channels (**AC**s) embedded within the deformable sensing skin. The speaker emits a continuous sound signal through the channels which the microphone will receive. When an external force deforms the sensing surface, these ACs also deform, resulting in a variation in the amplitude of the acoustic wave received by the microphone. The variation is then mapped into contact force and its contact location using Fast Fourier Transformation (FFT) and machine learning techniques. To prove the concept, we made simple prototypes of AST skin with a generic headphone speaker and microphone placed on either side of the skin. To enable the portability of the skin during the studies, we arranged them in a 3D-printed casing. In the future, we will develop application-based AST skins with the miniature speaker-mic unit and without a hard casing around the skin.

Previously, a few AST skin designs are prototyped and evaluated to test the following questions [22]: (i). Is the single channel enough to develop a skin requiring narrow sensing surfaces? (ii) Can this channel take a simple geometrical shape to distinguish forces with their contact locations when acted at different points on its length? (iii). Can multiple ACs can be used if it is required to have a broader sensing surface? (iv) Whether these ACs can have similar or dissimilar geometrical shapes? (v) What speaker-microphone arrangement is ideal for better skin performance?

To answer these, as a first attempt, we have used two simple AC geometries (cylinder and cone) and various speaker-microphone configurations. And to test the feasibility of using multiple ACs for broader skin, we started with a dual-channel configuration. We studied these parameters by considering three sensing points on the skin surface, 20 mm apart, as shown in Fig 3.

Preliminary findings[22]: We could draw the following inferences on the AST skin designs:

(a) AST-1

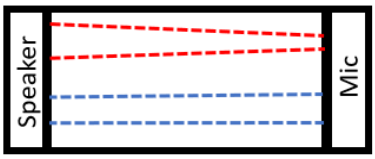

(b) AST-4d

Fig. 2: AST designs

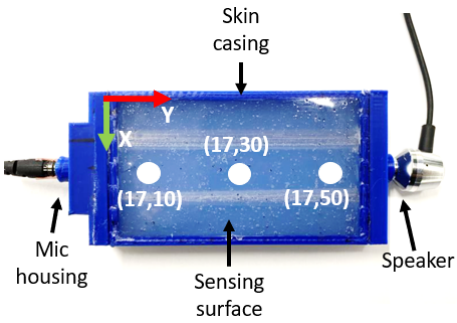

Fig. 3: AST-4d skin with three sensing points

- A single AC can measure forces and contact locations for skin that requires only a narrow sensing area.
- Single AC can have a simple cylindrical shape as it can differentiate forces and their contact location acting at different points on its length.
- The skin that may require a broader sensing area can use multiple channels with a single speaker for all channels. Also, this finding outlines the scope of scalability of AST skin as it doesn't require a separate speaker for each channel.
- While using multiple ACs, better performance is shown when the channels are of different geometrical shapes.

While analysing the performance of all these AST skin configurations, the skins AST-1 and AST-4d performed well (refer Fig 2). The configurations AST-1 (single channel design) and AST-4d (dual channel design) could make more than 93% of force measurements within ± 1.5 N tolerance (for a full-scale range of $0\text{-}30^{+1}$ N) and make contact location predictions with more than 96% accuracy.

Inspired by our preliminary findings, we select the skins AST-1 and AST-4d for further performance testing. Here, we study these skin's performance in predicting force and contact location within closer sensing points. As a step towards that, we consider nine sensing points 6 mm apart spanning the length of skin (refer Fig 4b).

A. Methodology

This section outlines the methodology adopted for calibrating the two AST skins with nine continuous sensing points

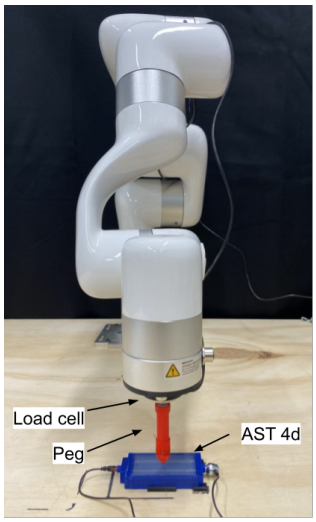

(a) Calibration setup

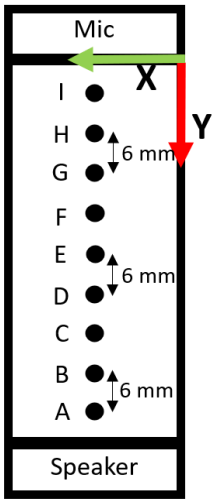

(b) 9 sensing points

Fig. 4: AST skin calibration

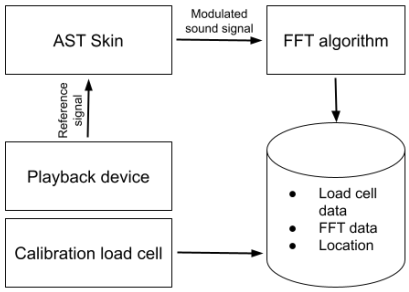

(a) Data processing pipeline

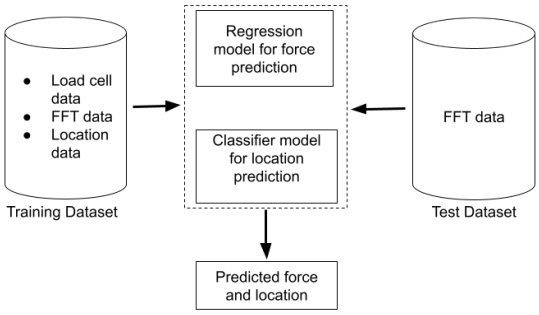

(b) Machine learning model for force and location estimation

Fig. 5: Tactile feature extraction method: we use a combined approach of FFT and ML to extract tactile features from the acoustic signals. Machine learning models learn the correlation between force and location and the change in the acoustic signal modulation captured by the microphone.

with a spatial resolution of 6 mm.

a) Sensor calibration: The calibration setup consists of a 6-degree-of-freedom robotic arm[1] mounted with a high-precision axial load cell measuring 0-1 KN. A peg is mounted to the load cell to make contact with the sensing point on the skin. The respective AST skin is placed on the worktable firmly, as shown in Fig 4a.

During the calibration process, the speaker continuously plays a reference signal. Here, we use a reference signal consisting of four sine waves with frequencies 300 Hz, 500 Hz, 700 Hz, and 900 Hz with an individual amplitude of 0.6 on a 0 to 1 scale.

The robotic arm is driven to the sensing points 'A' to 'I' individually. On each point, the arm pushes the peg vertically with an increment of 0.3 mm until the load cell reading reaches 30^{+2} N. After each increment, the microphone records 20 samples of the reference sound signal and labels with the corresponding force value and sensing point location.

Later, the reference signal recorded during each step is converted to the FFT data (amplitude of individual frequency components 300 Hz, 500 Hz, 700 Hz, 900 Hz) using the Fast Fourier Transform (FFT). And the final calibration data set will have load cell values, with the corresponding sensing point location and the FFT data. This calibration data set has 3600 data points generated for an AST skin, i.e., 400 data points per sensing point. The data processing pipeline adopted in the calibration process is shown in Fig 5a.

b) Tactile feature extraction method: The amplitude of the different frequency components (FFT data) changes as forces increase at each sensing location [22]. So for predicting the unknown forces and their contact locations at an instance, the corresponding FFT data is used. This is expressed as:

$$(Fi, Li) = f(A300i, A500i, A700i, A900i) \quad (1)$$

where *Fi* is the unknown force at an instance *i*, and *A300i, A500i, A700i, A900i* are the amplitude of frequency components 300 Hz, 500 Hz, 700 Hz, 900 Hz recorded at the same instance (FFT data), and *Li* is the location of contact.

We utilised Machine Learning (ML) techniques to estimate the force and contact location from FFT data (Fig 5b). We compared a range of regression and classifier models to predict unknown forces and contact locations. These models are trained with a calibration data set of respective skin with a data partition of 90:10 and a 10-fold cross-validation. For each skin, we selected the regression and classifier models that had the lowest validation error and the highest validation accuracy, respectively (see Tables I and II).

III. Results and Discussions

This section presents the skin performance in predicting the contact forces and their locations. And also discusses the skin performance when tested in a real-time pushing task.

A. Calibration performance

1) Contact force prediction: The force prediction results are presented as percentage predictions made within a tolerance of ± 1 to ± 5 N (refer Fig. 6). It has been studied that AST-4d provides better force predictions than AST-1. AST-4d could make 68.89% of the predictions within

[1]The UFactory xArm by ufactory.cc

TABLE I: Comparsion of Regression models for force prediction based on validation error

Regression models for force prediction	Validation Error (N)	
	AST-1	AST 4d
Linear Regression		
Linear	3.41	3.33
Interactions Linear	3.24	2.69
Robust	3.47	3.36
Stepwise Linear	3.25	2.69
Regression Trees		
Fine Tree	3	2.32
Medium Tree	2.82	2.24
Coarse Tree	2.86	2.42
Support Vector Machines		
Linear	3.5	3.37
Quadratic	3.29	2.68
Cubic	4.36	2.46
Fine Gaussian	2.73	1.98
Medium Gaussian	2.86	2.21
Coarse Gaussian	3.14	2.81
Gaussian Process		
Rational Quadratic	2.73	**1.73**
Squared Exponential	2.78	1.9
Matern 5/2	2.75	1.78
Exponential	2.59	1.71
Ensemble of Trees		
Boosted Trees	2.97	2.4
Bagged Trees	**2.57**	1.95
Neural Networks		
Narrow Neural	3.23	2.18
Medium Neural	2.88	1.94
Wide Neural Network	2.69	1.86
Bilayered Neural Network	2.75	1.94
Trilayered Neural Network	2.78	1.92

± 1 N tolerance, but it is 50% in the case of AST-1. This difference in performance continues when analysing the force predictions for other tolerance ranges. From this, it can be inferred that a better force prediction performance can be obtained for closer sensing points by increasing the number of ACs and when these channels have different geometrical shapes.

2) Contact location prediction: Tables III, IV and V summarise the contact location prediction results. From the results, AST-4d performed slightly better while making true location predictions and within $\pm$ 6mm spatial resolution. AST-1 can predict true locations with 62.94% accuracy and locations with $\pm$ 6mm resolution at 75.55% accuracy. For AST-4d, they are 64.16% and 84.16%, respectively. Therefore, regarding location prediction capability, skin with multiple ACs with different geometries again showed its potential.

So, from both force and location prediction results, we can infer that for improving the spatial resolution of sensing points on AST skin, using multiple ACs with different geometrical shapes can be adopted. And we call the AST-4d a possible C-AST configuration, as it can provide continuous sensing points on the sensing surface.

B. Real-time testing of the AST-4d skin

To further analyse the performance of skin design with multiple and geometrically different channels, we did a pushing experiment with AST-4d skin. We also aim to

TABLE II: Comparsion of Classifier models for contact location prediction based on validation accuracy

Classifier models for location prediction	Validation Accuracy(%)	
	AST-1	AST 4d
Tree		
Fine Tree	45.2	45.2
Medium Tree	25.5	31.3
Coarse Tree	17.6	22.9
Discriminant Analysis		
Linear Discriminant	26.7	32.9
Quadratic Discriminant	26.5	39.3
Naïve Bayes Classifiers		
Guassian Naïve Bayes	16.5	22.7
Kernal Naïve Bayes	27.7	31.2
Support Vector Machines		
Linear SVM	27.1	38.2
Quadratic	49.8	54.1
Cubic	xx	52.1
Fine Guassian	57.4	66.3
Medium Guassian	45.1	55.7
Coarse Guassian	23.3	37.5
Nearest Neighbor Classifier		
Fine KNN	58.3	65.3
Medium KNN	51.8	64.2
Coarse KNN	32.8	44.8
Cosine KNN	37.8	53
Cubic KNN	50.2	64.5
Weighted KNN	59	**67.3**
Ensemble Classifiers		
Boosted Trees	26	32.8
Bagged Trees	**63.2**	64.3
Subspace Discriminant	21.8	31.6
Subspace KNN	51.1	44.7
RUSBossted Trees	23.8	31.9
Neural Network Classifiers		
Narrow NN	55.1	55.3
Medium NN	60.1	61.9
Wide NN	63.3	65.4
Bilayered NN	58	58.7
Trilayered NN	57.7	59

TABLE III: AST-1 - Predicted contact location (Loc_P) Vs True location (Loc_T) for 40 test cases per sensing points

Loc	A_P	B_P	C_P	D_P	E_P	F_P	G_P	H_P	I_P
A_T	28	0	1	2	1	2	2	3	1
B_T	1	29	3	1	1	1	1	1	2
C_T	0	3	26	2	2	2	3	1	1
D_T	0	3	3	22	2	4	3	1	2
E_T	0	0	0	1	38	1	0	0	0
F_T	1	0	5	6	2	16	4	4	2
G_T	2	0	3	2	0	8	17	5	3
H_T	2	0	1	3	1	2	5	26	0
I_T	0	1	0	3	1	1	4	9	21

TABLE IV: AST-4d - Predicted contact location (Loc_P) Vs True location (Loc_T) for 40 test cases per sensing points

Loc	A_P	B_P	C_P	D_P	E_P	F_P	G_P	H_P	I_P
A_T	19	7	3	1	2	3	3	1	1
B_T	12	22	1	3	1	0	0	1	0
C_T	1	3	29	4	2	0	1	0	0
D_T	0	1	8	25	2	2	1	1	0
E_T	0	0	2	2	29	5	0	2	0
F_T	0	0	3	2	3	22	6	2	2
G_T	1	0	0	3	0	4	25	6	1
H_T	0	2	3	0	0	1	4	28	2
I_T	0	4	0	0	0	0	1	3	32

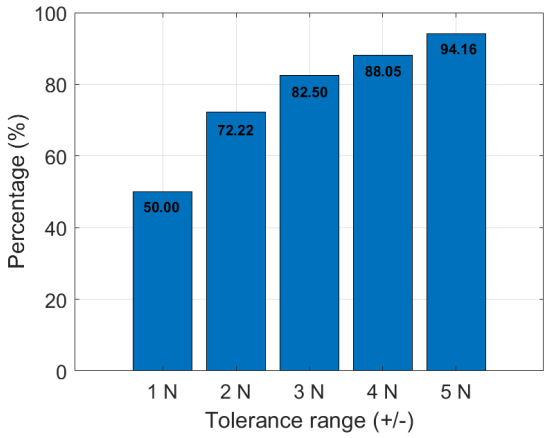

(a) AST-1

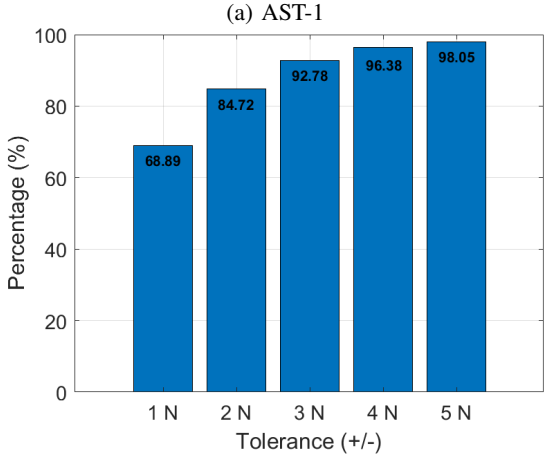

(b) AST-4d

Fig. 6: Percentage of force predictions made within ± 1 N to ± 5 N

compare its sensing performance with an off-the-shelf soft tactile sensor (Xela uSkin[2]). During this experiment, the AST skin is fastened to an extension attached to the robot arm to push a box fixed on the work table. We have provided an axial load cell attached to the box with a peg connected to it. The peg confirms the contact of the sensor surface during the pushing action. The load cell measures the interaction forces during the pushing and is compared with the AST skin reading. A normal static load of 5 N, 10 N, and 15 N is applied to the box by driving the robot arm through the peg. In the first instance, the peg makes contact with the center of the sensing surface of AST-4d skin (point E). Later we change this contact point to D (top) and F (bottom), which are at 6 mm resolution (refer Fig 4b). We applied these forces at each point and recorded ten readings. The same experiment is repeated with the Xela sensor starting from the center of its sensing area to two points at $\pm$6mm (refer Fig 8). Before we did this experiment, we re-calibrated the AST-4d skin.

Table VI presents the mean error in force measurements obtained from the AST-4d skin and the Xela sensor, along

[2]xelarobotics.com

TABLE V: Average accuracy of true location prediction and with $\pm$6mm resolution

Sensing points	AST-1 prediction		AST 4d prediction	
	True	$\pm$6 mm resolution	True	$\pm$6 mm resolution
A	70	70	47.5	65
B	72.5	82.5	55	87.5
C	65	77.5	72.5	90
D	55	67.5	62.5	87.5
E	95	100	72.5	90
F	40	55	55	77.5
G	42.5	75	62.5	87.5
H	65	77.5	70	85
I	52.5	75	80	87.5
Average	61.94	75.55	64.16	84.16

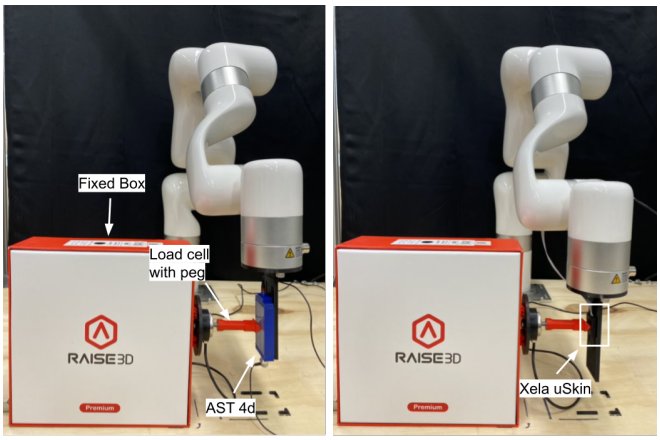

(a) AST skin (b) Xela uSkin

Fig. 7: Testing experimental setup: A uFactory 6DOF robotic arm is used to test C-AST. This figure shows the real-time pushing experiment with (a) C-AST skin and (b) Xela uSkin. A load cell (measuring range: 1 to 1 KN, resolution: 0.0001 N) is attached to the box to be pushed. The tactile sensors are attached to the robot's wrist while pushing against the load cell from right to left.

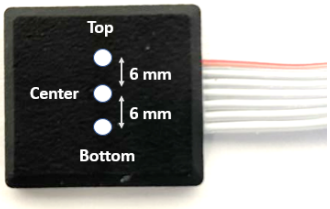

Fig. 8: Front view of the Xela USkin sensor and the locations considered real-time testing in Fig. 7. The Xela uSkin has 4x4 tactile cells (taxel) each providing normal and shear x and shear y readings. The company provides the calibration for the sensor.

with their respective standard deviations. The results show that the AST-4d skin outperforms the Xela sensor in measur-

TABLE VI: Error in force measured by AST-4d and Xela sensor during the pushing experiment (standard deviation in brackets)

Locations	**True value (N)**	**Mean error (N)**	
		AST-4d	Xela
Top	5	-0.50 (0.54)	1.63 (0.10)
	10	-0.50 (0.78)	1.39 (0.02)
	15	-0.34 (0.99)	9.83 (0.06)
Center	5	-1.06 (0.68)	2.67 (0.02)
	10	-0.15 (0.81)	3.99 (0.04)
	15	0.12 (1.09)	11.55 (0.16)
Bottom	5	0.42 (0.63)	2.01 (0.03)
	10	0.85 (0.70)	1.44 (0.27)
	15	1.87 (1.49)	-0.46 (0.08)

ing pushing forces at all test points, with a relatively lower error. Among all sensing points, the maximum mean error recorded by the AST-4d skin is 1.87 N at point F, while the Xela sensor yields better performance at the bottom sensing point with a maximum mean error of 2.01 N across all other sensing points. This could be attributed to the fact that the load cell peg had better contact with the taxels at this bottom point than in other locations. In contrast, the AST-d skin relies on channel deformations rather than a specific taxel activation, which could contribute to its superior performance in this scenario. Overall, these findings suggest that the AST-4d skin is a promising configuration for C-AST which can provide accurate and reliable force sensing.

IV. Conclusions

This study demonstrates that the proposed AST skin technology can be used for high-resolution tactile readings. We evaluated two AST skin designs (dual and single-channel design) to predict the normal contact forces and their locations. It was found that the dual-channel design surpassed the single-channel design in terms of force and contact location prediction accuracy. Moreover, our study results indicate that the performance of the AST skin can be further improved by increasing the number of channels and with different geometrical shapes. We believe that AST skin technology has the potential to revolutionise the field of tactile sensing, as it can be built at a low cost and exhibits good measurement capabilities.

Our future work will include extending the skin sensing area with 2-D sensing points and improving the spatial resolution by investigating different channel topologies and configurations. We will also investigate how C-AST can measure shear forces. Moreover, we intend to utilise this sensor technology for applications such as strawberry picking and breast cancer examination [23].

References

[1] H. Zheng, Y. Jin, H. Wang, and P. Zhao, "Dotview: A low-cost compact tactile sensor for pressure, shear, and torsion estimation," *IEEE Robotics and Automation Letters*, vol. 8, no. 2, pp. 880–887, 2023.

[2] M. Lambeta, P.-W. Chou, S. Tian, B. Yang, B. Maloon, V. R. Most, D. Stroud, R. Santos, A. Byagowi, G. Kammerer *et al.*, "Digit: A novel design for a low-cost compact high-resolution tactile sensor with application to in-hand manipulation," *IEEE Robotics and Automation Letters*, vol. 5, no. 3, pp. 3838–3845, 2020.

[3] Z. Kappassov, J.-A. Corrales, and V. Perdereau, "Tactile sensing in dexterous robot hands," *Robotics and Autonomous Systems*, vol. 74, pp. 195–220, 2015.

[4] J. Zimmer, T. Hellebrekers, T. Asfour, C. Majidi, and O. Kroemer, "Predicting grasp success with a soft sensing skin and shape-memory actuated gripper," in *2019 IEEE/RSJ International Conference on Intelligent Robots and Systems (IROS)*. IEEE, 2019, pp. 7120–7127.

[5] Q. Li, Z. Ullah, W. Li, Y. Guo, J. Xu, R. Wang, Q. Zeng, M. Chen, C. Liu, and L. Liu, "Wide-range strain sensors based on highly transparent and supremely stretchable graphene/ag-nanowires hybrid structures," *Small*, vol. 12, no. 36, pp. 5058–5065, 2016.

[6] K. Song, S. H. Kim, S. Jin, S. Kim, S. Lee, J.-S. Kim, J.-M. Park, and Y. Cha, "Pneumatic actuator and flexible piezoelectric sensor for soft virtual reality glove system," *Scientific reports*, vol. 9, no. 1, p. 8988, 2019.

[7] M. Rehan, M. M. Saleem, M. I. Tiwana, R. I. Shakoor, and R. Cheung, "A soft multi-axis high force range magnetic tactile sensor for force feedback in robotic surgical systems," *Sensors*, vol. 22, no. 9, p. 3500, 2022.

[8] H. Wu, B. Zheng, H. Wang, and J. Ye, "New flexible tactile sensor based on electrical impedance tomography," *Micromachines*, vol. 13, no. 2, p. 185, 2022.

[9] B. Ward-Cherrier, N. Pestell, L. Cramphorn, B. Winstone, M. E. Giannaccini, J. Rossiter, and N. F. Lepora, "The tactip family: Soft optical tactile sensors with 3d-printed biomimetic morphologies," *Soft robotics*, vol. 5, no. 2, pp. 216–227, 2018.

[10] D. F. Gomes and S. Luo, "Geltip tactile sensor for dexterous manipulation in clutter," in *Tactile Sensing, Skill Learning, and Robotic Dexterous Manipulation*. Elsevier, 2022, pp. 3–21.

[11] W. Yuan, S. Dong, and E. H. Adelson, "Gelsight: High-resolution robot tactile sensors for estimating geometry and force," *Sensors*, vol. 17, no. 12, p. 2762, 2017.

[12] E. Donlon, S. Dong, M. Liu, J. Li, E. Adelson, and A. Rodriguez, "Gelslim: A high-resolution, compact, robust, and calibrated tactile-sensing finger," in *2018 IEEE/RSJ International Conference on Intelligent Robots and Systems (IROS)*. IEEE, 2018, pp. 1927–1934.

[13] D. Gong, R. He, J. Yu, and G. Zuo, "A pneumatic tactile sensor for co-operative robots," *Sensors*, vol. 17, no. 11, p. 2592, 2017.

[14] C.-H. Chuang, H.-K. Weng, J.-W. Chen, and M. O. Shaikh, "Ultrasonic tactile sensor integrated with tft array for force feedback and shape recognition," *Sensors and Actuators A: Physical*, vol. 271, pp. 348–355, 2018.

[15] H. Shinoda, K. Matsumoto, and S. Ando, "Acoustic resonant tensor cell for tactile sensing," in *Proceedings of International conference on Robotics and Automation*, vol. 4. IEEE, 1997, pp. 3087–3092.

[16] Y. Tanaka, T. Fukuda, M. Fujiwara, and A. Sano, "Tactile sensor using acoustic reflection for lump detection in laparoscopic surgery," *International journal of computer assisted radiology and surgery*, vol. 10, pp. 183–193, 2015.

[17] K. Teramoto and K. Watanabe, "Acoustical tactile sensor utilizing multiple reflections for principal curvature measurement," in *SICE 2001. Proceedings of the 40th SICE Annual Conference. International Session Papers (IEEE Cat. No. 01TH8603)*. IEEE, 2001, pp. 339–344.

[18] K. Park, H. Yuk, M. Yang, J. Cho, H. Lee, and J. Kim, "A biomimetic elastomeric robot skin using electrical impedance and acoustic tomography for tactile sensing," *Science Robotics*, vol. 7, no. 67, p. eabm7187, 2022.

[19] E. Fujiwara and L. de Oliveira Rosa, "Agar-based soft tactile transducer with embedded optical fiber specklegram sensor," *Results in Optics*, vol. 10, p. 100345, 2023.

[20] V. Wall, G. Zöller, and O. Brock, "Passive and active acoustic sensing for soft pneumatic actuators," *arXiv preprint arXiv:2208.10299*, 2022.

[21] G. Zöller, V. Wall, and O. Brock, "Acoustic sensing for soft pneumatic actuators," in *2018 IEEE/RSJ International Conference on Intelligent Robots and Systems (IROS)*. IEEE, 2018, pp. 6986–6991.

[22] V. R. S, W. Mandil, S. Parsons, and A. G. E, "Acoustic soft tactile skin (ast skin)," *arXiv, 2303.17355*, 2023.

[23] O. Sanni, G. Bonvicini, M. A. Khan, P. C. López-Custodio, K. Nazari *et al.*, "Deep movement primitives: toward breast cancer examination robot," in *Proceedings of the AAAI Conference on Artificial Intelligence*, vol. 36, no. 11, 2022, pp. 12 126–12 134.